

Geometrical aspects of turbulent/non-turbulent interfaces with and without mean shear

Tomoaki Watanabe,^{1,2,a)} Carlos B. da Silva,^{1,2} Koji Nagata,¹ and Yasuhiko Sakai³

¹Department of Aerospace Engineering, Nagoya University, Nagoya, Japan

²LAETA, IDMEC, Instituto Superior Técnico, Universidade de Lisboa, Lisboa, Portugal

³Department of Mechanical Science and Engineering, Nagoya University, Nagoya, Japan

(Received 28 February 2017; accepted 12 July 2017; published online 9 August 2017)

The geometry of turbulent/non-turbulent interfaces (TNTIs) arising from flows with and without mean shear is investigated using direct numerical simulations of turbulent planar jets (PJET) and shear free turbulence (SFT), respectively, with Taylor Reynolds number of about $Re_\lambda \approx 100$. In both flows, the TNTI is preferentially aligned with the tangent to the TNTI displaying convex, where the turbulent fluid nearby tends to have a stronger enstrophy, more frequently than concave shapes. The different flow configurations are reflected in different orientations of the TNTI with respect to the flow direction (and its normal). While the interface orientation with respect to the mean flow direction in PJET has an influence on the velocity field near the TNTI and the enstrophy production in the turbulent sublayer, there is no particular discernible dependence on the interface orientation in SFT. Finally, the intense vorticity structures or “worms,” which are possibly associated with “nibbling” entrainment mechanism, “feel” the local geometry of the TNTI, and it is shown that in PJET, a smaller local radius of these structures arises in regions near the TNTI where the local TNTI faces the mean flow direction. *Published by AIP Publishing.* [<http://dx.doi.org/10.1063/1.4996199>]

I. INTRODUCTION

Turbulence in the environment and in engineering devices is often localized and surrounded by a non-turbulent flow, where the localized turbulence is separated from the outside by an interfacial layer: the so-called turbulent/non-turbulent interface (TNTI). The flow dynamics near the TNTI is crucial in various phenomena involving turbulent mixing and entrainment, e.g., localized turbulent spots are observed in ocean mixed layers,^{1,2} atmospheric boundary layers,³ and volcanic eruptions.⁴ The flow properties dramatically change across the TNTI, where important exchanges of mass, momentum, energy, and chemical species occur between the turbulent and non-turbulent flow regions. Modeling the entrainment mechanism is therefore very important for the prediction of many environmental and engineering flows since the flow evolution is often governed by the entrainment rate.⁵ In this context, understanding the geometrical characteristics such as the surface area and curvature and how the turbulent scales and structures affect these characteristics can be very useful, e.g., the surface area between two fluids or two fluid streams is one of the leading parameters dictating overall fluid exchanges at these interfaces.

TNTIs have been studied using canonical flows such as mixing layers, wakes, jets, and boundary layers. It has been observed that the TNTI is a finite thickness layer composed of a viscous superlayer (VSL), where enstrophy growth is dominated by viscous diffusion, and a turbulent

sublayer (TSL), where enstrophy production becomes important.⁶ Many recent studies have focused on the flow dynamics near TNTIs; however, only relatively few works have been devoted to the study of its geometry. Notable exceptions are Refs. 7–10.

Observations of the TNTI have long time ago shown that this interface is sharp and is continually distorted by a wide range of scales from the turbulent region,^{11,12} and in particular, the largest convolutions at the TNTI are the imprint of the largest-scale eddies from the turbulent region.¹² It has been observed that the probability density function (pdf) of the position of the TNTI is approximately Gaussian.^{7,11,13–15} However, the TNTI presents different forward and backward geometrical characteristics, e.g., slopes, in some flows, such as in wakes.¹⁶ The convex and concave regions of the TNTI have also been linked with different local entrainment velocities^{8,17,18} and possibly reflect the characteristics of the intense eddy structures nearby.¹⁹ Specifically, the vorticity jump at the TNTI observed in different flows is imposed by the eddy structure near the TNTI,^{7,20} while the dynamics of the small-scale intense vorticity structures (IVSs) neighboring the TNTI suggests that the nibbling eddy motions are linked to the diffusion of vorticity from these small-scale motions near the TNTI.²¹ Finally, the fractal features of the TNTI have been measured in a number of studies, where a fractal dimension between $D_2 \approx 2.3$ – 2.4 has been observed.^{9,22,23}

In the present work, we focus on the geometry of the TNTI by analyzing its outer envelope known as the irrotational boundary (IB). In order to analyze possible effects from the existence of mean shear, two different flows are

^{a)}watanabe.tomoaki@c.nagoya-u.jp

analyzed: shear free turbulence (SFT) and turbulent planar jets (PJET). As will be shown below, even though we do not use the Reynolds decomposition in most of the subsequent analysis, the instantaneous fields and TNTI characteristics do show the imprint of the mean shear, which is determined by the different flows/initial conditions.

We start by investigating the interface geometry represented by the local curvature and interface orientation, and we proceed by investigating the local geometry of the TNTI in connection with the enstrophy dynamics and the relative fluid velocity near the TNTI. Wolf *et al.*¹⁷ investigated the role of the mean and Gaussian curvatures in the local entrainment velocity,²⁴ which was determined right at the IB, and they showed that the local entrainment is more sensitive to the mean curvature than to the Gaussian curvature. Therefore, here we use the mean curvature for distinguishing the IB shape. However, unlike Wolf *et al.*,¹⁷ where the dependence of the vorticity dynamics on the curvature is investigated at the outer edge of the TNTI, we investigate the enstrophy production in the turbulent sublayer since the enstrophy production is almost negligible at the IB.

This paper is organized as follows. Section II describes the direct numerical simulations (DNSs) of SFT and PJET and the procedures used to compute statistics in this work. Section III addresses the geometry of the IB and its relation with the enstrophy production and with the local entrainment velocity near the TNTI. Section IV analyzes the relation between the interface geometry and the characteristics of the intense vorticity structures. Section V discusses different dependence of the TNTI on the geometry observed between SFT and PJET. The article ends in Sec. VI with an overview of the main results and conclusions.

II. DIRECT NUMERICAL SIMULATION

A. Direct numerical simulations of shear free turbulence and planar turbulent jets

The TNTI is investigated in a shear-free turbulence²⁵ (SFT) and a temporally developing planar jet²⁶ (PJET). We performed DNS of these flows using a DNS code whose details were described in previous studies.^{21,26} The DNS uses pseudo-spectral methods for spatial discretization and a 3rd-order, 3-step Runge–Kutta method for temporal advancement, and the simulations are fully de-aliased using the 3/2 rule. The DNSs are carried out in a periodic box, with the origin of the coordinate system $(x, y, z) = (0, 0, 0)$ placed at the center of the computational domain. It was confirmed that the periodic boundaries have no influence on the development of the SFT and PJET, provided that the computational box is large enough as is the case here.

In the SFT simulations, the computational domain, whose size is $2\pi \times 2\pi \times 2\pi$ is represented by $(N_x \times N_y \times N_z) = (512 \times 512 \times 512)$ collocation points. Initially, a DNS of forced homogeneous isotropic turbulence (HIT) is carried out, and subsequently, a shear free boundary between the turbulent and the non-turbulent flows is generated by instantaneously

inserting this initial HIT into the middle of a quiescent flow. The initial field from HIT is taken from the center of the computational domain ($|y| \leq 0.7\pi$), while the non-turbulent flow with initially zero velocity is in the remaining domain ($0.7\pi \leq |y| \leq \pi$). The turbulent flow then spreads into the non-turbulent flow region in the absence of mean shear. Further details on the procedure used to generate SFT are described in previous works.²⁵

The PJET simulation is carried out in a computational domain with sizes $L_x = 7.5h$, $L_y = 10h$, and $L_z = 7.5h$ in the streamwise (x), lateral (y), and spanwise (z) directions, respectively, where h is the inlet nozzle width of the jet, and the number of grid points is $(N_x \times N_y \times N_z) = (768 \times 1024 \times 768)$. As in similar DNS of temporally developing planar jets,^{26,27} the initial velocity profiles are generated by superimposing a “spectral noise”²⁸ to the mean velocity profile given by a hyperbolic tangent function. The initial mean streamwise velocity at the center of the jet ($y=0$) is U_1 , and no co-flow is added outside of the jet. The initial Reynolds number is $Re = U_1 h / \nu = 6000$, where ν is the kinematic viscosity. Further details on the PJET simulation are described in Refs. 21 and 26. DNSs at a higher Reynolds number are already available for planar jets.²⁹ However, we have used the same Reynolds number for the jet and for SFT in order to be able to compare the two flows. Nevertheless, the Reynolds number $Re_\lambda \approx 100$ is sufficiently high for the flows to be considered as representatives of high Reynolds number turbulence in the sense that the dissipation law is observed.

The TNTI is investigated using one single instantaneous field in the DNS of the PJET and SFT. The Taylor-based Reynolds number is $Re_\lambda = u_{\text{rms}} \lambda_x / \nu = 100$ and 98, at the center of the SFT and PJET, respectively, where u_{rms} is the rms velocity in the x direction and λ_x is the Taylor microscale calculated as $\lambda_x = \sqrt{\langle u^2 \rangle / \langle (\partial u / \partial x)^2 \rangle}$. Here, $\langle \rangle$ is the conventional mean value, which is computed by taking averages on a x – z plane at each lateral location, and $u = U - \langle U \rangle$ is the velocity fluctuation in x direction. The ratio between λ_x and the Kolmogorov scale $\eta = (\nu^3 / \epsilon)^{1/4}$ is $\lambda_x / \eta = 19.5$ and 19.6 at $y = 0$ in the SFT and PJET, respectively, where ϵ is the dissipation rate of turbulent kinetic energy in the turbulent core region, and the resolution at $y = 0$ is 1.41η and 1.35η in SFT and PJET, respectively.

B. TNTI detection and conditional statistics

As mentioned in the Introduction, the TNTI layer consists of two (sub)layers: the turbulent sublayer (TSL) and viscous superlayer (VSL),⁶ where the latter forms at the outer edge of the TNTI.³⁰ As in previous studies on the TNTI,^{26,31} the iso-surface of the vorticity magnitude $|\omega| = \omega_{\text{th}}$ is used to detect the *irrotational boundary* (IB),³² which delimits the outer surface of the TNTI layer. The actual value of ω_{th} is determined by the dependence of the detected turbulent volume on ω_{th} ,³³ and as in previous studies, we confirmed that this method works very well in both SFT and PJET.¹⁴

Once the IB is detected, conditional statistics in relation to the TNTI (or the IB) can be computed and the present work uses the same procedure to compute these statistics as previously

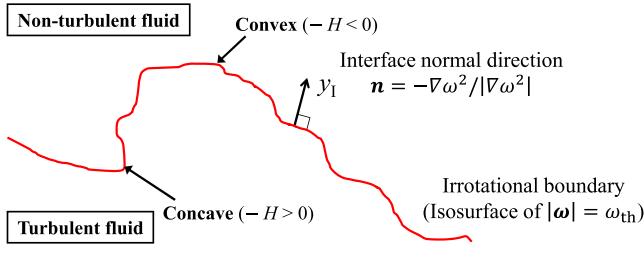


FIG. 1. Definition of the local coordinate axis y_1 fixed at the irrotational boundary (IB) used for calculating the conditional statistics in relation to the TNTI. Examples of concave and convex interface shapes, distinguished through the large-scale mean curvature H , are also shown. The interface normal vector and mean curvature are calculated using the three-dimensional (space) direction components.

described³² (see Fig. 1): We introduce a local coordinate y_1 , whose origin is located at the (local) IB, where y_1 is normal to the TNTI and points into the non-turbulent region. Because the IB is an iso-surface with constant enstrophy $\omega^2/2 = \omega_i\omega_i/2$, the boundary normal direction is given by the unit normal vector $\mathbf{n} = -\nabla\omega^2/|\nabla\omega^2|$ at the IB. Thus, the turbulent and irrotational regions are defined by $y_1 < 0$ and $y_1 > 0$, respectively. In this work, the distance to the IB is normalized by the Taylor microscale $\lambda = (\lambda_x + \lambda_y + \lambda_z)/3$ and/or the Kolmogorov scale η , taken from the center of the turbulent core region ($y = 0$), where $\lambda_i = \sqrt{\langle u_i^2 \rangle / \langle (\partial u_i / \partial x_i)^2 \rangle}$ is the Taylor microscale for the direction i . The conditional average on y_1 is denoted by $\langle \cdot \rangle_{y_1}$.

In the present work, the interface geometry is studied in terms of its local curvature and orientation. Specifically, the mean curvature of the enstrophy iso-surface is defined with the outward normal vector \mathbf{n} of the IB as $H = \nabla \cdot \mathbf{n}/2$, where $-H < 0$ and $-H > 0$ represent a convex and a concave shape, respectively (see Fig. 1). Notice that the present definition of H is symmetrical to the one used by Wolf *et al.*^{8,17} because y_1 in Fig. 1 points toward the non-turbulent region following the work of Bisset *et al.*³¹ For comparisons with previous studies on the shape of the TNTI where the curvature was defined with the inward normal vector (i.e., $-\mathbf{n}$), we show the results with $-H$. In order to remove small scale numerical noise from these results and also because we intend to focus mainly on the large scale geometrical features of the TNTI, associated with the large-scale vorticity, a box filter

with filter size $\Delta = 0.5\lambda$ was applied to the enstrophy field, prior to the computation of the vector normal to the interface. Therefore, in the remainder of this work, the interface curvature is actually the large-scale mean curvature defined by $H \equiv \nabla \cdot \mathbf{n}_{LS}/2$, where $\mathbf{n}_{LS} \equiv -\nabla\omega^2/|\nabla\omega^2|$ and $\bar{\omega}^2$ is a low-pass-filtered value of ω^2 as described above. The results show that the filter size used here ($\Delta = 0.5\lambda$) is large enough to eliminate the small-scale convex and concave shapes resulting from numerical noise, but small enough to capture the large-scale convex and concave shapes associated with the large-scale eddies. We moreover confirmed that the results hardly change when filter widths slightly larger than from $\Delta = 0.5\lambda$ are considered.

III. RESULTS

A. Enstrophy transport near the TNTI

The fundamental characteristics of the TNTI can be examined by using the conditional profile of enstrophy $\omega^2/2 = \omega_i\omega_i/2$ and the conditional enstrophy budget, which is represented by the enstrophy transport equation,

$$\frac{D\omega^2/2}{Dt} = \omega_i S_{ij} \omega_j + \nu \nabla^2(\omega^2/2) - \nu \nabla \omega_i \cdot \nabla \omega_i. \quad (1)$$

The first, second, and third terms on the right-hand side of Eq. (1) represent the production (P_ω), viscous diffusion (D_ω), and viscous dissipation (ϵ_ω), respectively, where ω_i and S_{ij} are the vorticity vector $\omega_i = \epsilon_{ijk} \partial u_k / \partial x_j$ and the rate of strain tensor $S_{ij} = (\partial u_i / \partial x_j + \partial u_j / \partial x_i)/2$, respectively.

Figures 2(a) and 2(b) show the conditional averages of $\omega^2/2$, P_ω , D_ω , and ϵ_ω for SFT and PJET, respectively. The conditional profiles for SFT and PJET are very similar to previous studies on the TNTI.^{30,32} Near the IB ($y_1 = 0$), the enstrophy growth arises from the viscous diffusion and the inviscid enstrophy production is negligible. This region is the so-called viscous superlayer (VSL). After the VSL, the enstrophy production increases into the turbulent core region and becomes the dominant term marking the so-called turbulent sublayer (TSL). Finally, in the turbulent core region, the enstrophy dissipation roughly balances the production.

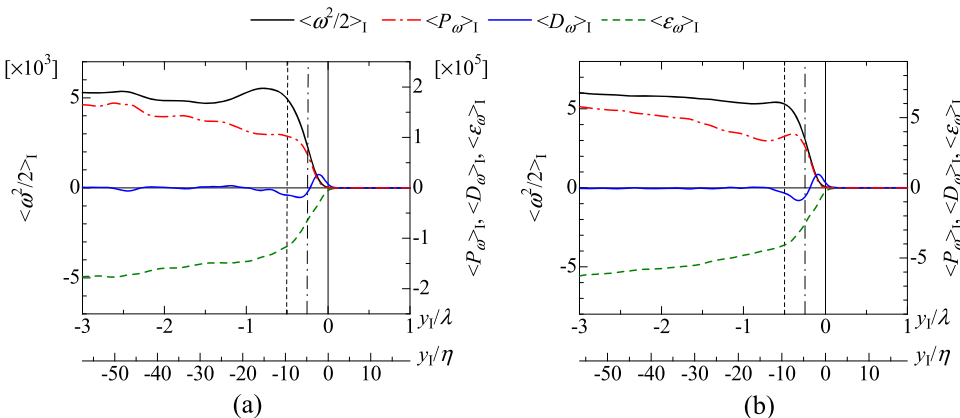


FIG. 2. Conditional mean enstrophy ($\omega^2/2$) and conditional average of production (P_ω), diffusion (D_ω), and dissipation (ϵ_ω) terms in the enstrophy transport equation in (a) SFT and (b) PJET. The vertical broken and dashed-dotted lines indicate $y_1/\lambda = -0.5$ and -0.25 , respectively. The interface characteristics are investigated in detail at $y_1/\lambda = -0.5$ and the turbulent fluid motion relative to the irrotational boundary movement at $y_1/\lambda = -0.5$ is used for the analysis. For comparison, y_1 normalized by the Kolmogorov scale η is also shown.

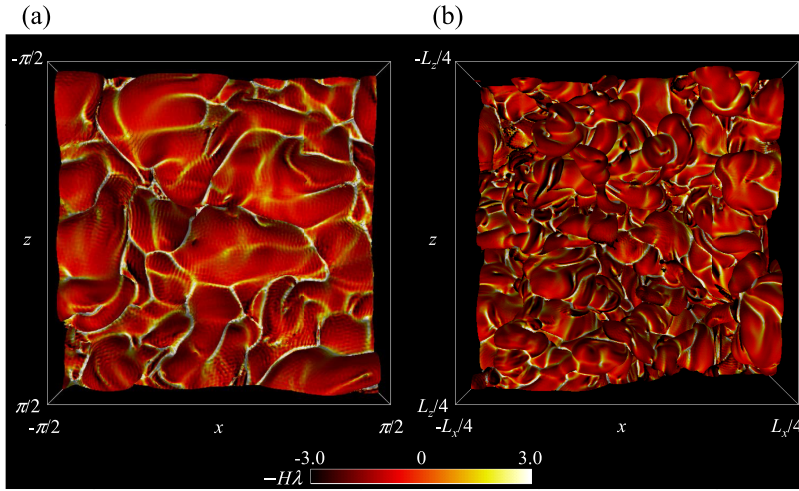


FIG. 3. Visualization of the irrotational boundary in (a) SFT and (b) PJET. The color depicts the large-scale mean curvature $H \equiv \nabla \cdot \mathbf{n}_{LS}/2$ normalized by the Taylor microscale $\lambda = (\lambda_x + \lambda_y + \lambda_z)/3$ taken from the center of the turbulent core region ($y = 0$). The barely visible high frequency oscillations are likely caused by a small effect of the Gibbs phenomenon, which is here visible because of the very small vorticity threshold defining the IB. The effect of these oscillations is not discernible in the statistics of the results obtained.

B. Geometric characteristics of the irrotational boundary

Figure 3 shows the IB in SFT and PJET defined through iso-surfaces of constant enstrophy $|\omega| = \omega_{th}$ and the color contours at the surfaces represent the large-scale mean curvature H , normalized by λ at $y = 0$. The IB shows a characteristic hilly surface that has been observed in several previous works²⁷ and whose large scales are caused by the large-scale eddies from the turbulent core region. The concave and convex boundary shapes related to the large-scale convolutions are also well distinguished through H and show a predominance of convex ($-H < 0$) over concave ($-H > 0$) curvatures in both flow types. The size of the large-scale convolutions observed in the SFT case also seems to be larger than in PJET, which is probably explained by the bigger integral scales in SFT compared with the box shown in the figures.

Figure 4 shows the probability density function (pdf) of $-H$ at the IB. The maximum of the pdf appears around $-H\lambda = -1$ (convex) while large and positive values of $-H$ also exist, and the pdf is positively skewed. This agrees with the visualizations of the IB in Fig. 3, in which the greatest part of the IB area displays negative values of $-H$, although large positive values appear on thin lines, occupying a very small surface area. This also agrees with the dominating idea that the IB and the TNTI are largely formed at the outer edge of the vortical structures²⁰ and explains how the largely

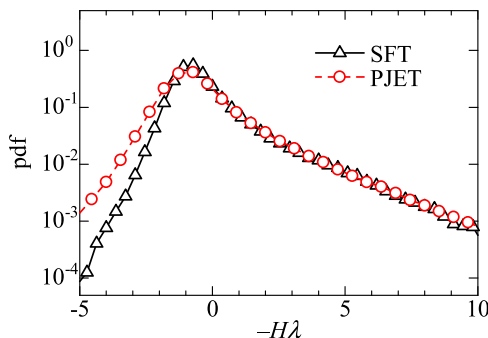


FIG. 4. Pdf of large-scale mean curvature $H \equiv \nabla \cdot \mathbf{n}_{LS}/2$ of the irrotational boundary in the SFT and PJET.

convex shape of the IB can be related to the shape of the vortical structures underneath its surface. The fact that concave zones appear to separate large-scale convex regions is also consistent with the presence of different large-scale vortical structures.

The orientation of the IB can be appreciated by analyzing the unit normal vector to the IB, here denoted by $\mathbf{n} = (n_x, n_y, n_z)$, as shown in Fig. 5 through the joint pdf of (n_x, n_y) at the irrotational boundary in the SFT and PJET. Note that the joint pdf includes information on the three components of \mathbf{n} because $n_x^2 + n_y^2 + n_z^2 = 1$ and we cannot statistically distinguish between the z and $-z$ directions. The spanwise component $|n_z|$ is represented by $\cos \theta$, where θ is the angle between \mathbf{n} and the z direction, and $\cos \theta \equiv |n_z| = \sqrt{1 - n_x^2 - n_y^2}$ for $\theta = 30^\circ, 60^\circ$, and 90° are shown by white broken lines.

In the DNS of SFT, the x and z directions are statistically equivalent. Since the joint pdf maps for large $|n_y|$, the most frequent orientation corresponds to the IB normal facing the y direction. In contrast, in the PJET case, the IB faces several different orientations with a similar probability, which is consistent with its shape being more corrugated. Thus, the orientation of the IB in SFT and PJET is different, which probably reflects the effects of the different eddy structure underneath the IB in both flows, which is indirectly related to the effects of the presence (or lack) of mean shear in the two flows.

To complete the assessment of the IB geometry, the joint pdf between the mean curvature of the IB and the nearby enstrophy, taken from $y_1/\lambda = -0.25$ (i.e., from the TSL region), is shown in Fig. 6. When the IB has a convex shape, the enstrophy nearby tends to be stronger. This is particularly true near convex shapes with $-H\lambda \approx -1$. Conversely when the local IB has a concave shape ($-H > 0$), the neighboring TSL region tends to display smaller enstrophy levels.

The relatively intense enstrophy levels observed near convex-shaped regions of the IB can be explained also by recalling that the local shape of the IB is imposed by the presence of the nearby vortical structures and their associated (approximately cylindrical) geometry. If the convex shape in the IB forms around the vortex structures, it is natural to find a locally strong vorticity near these regions since

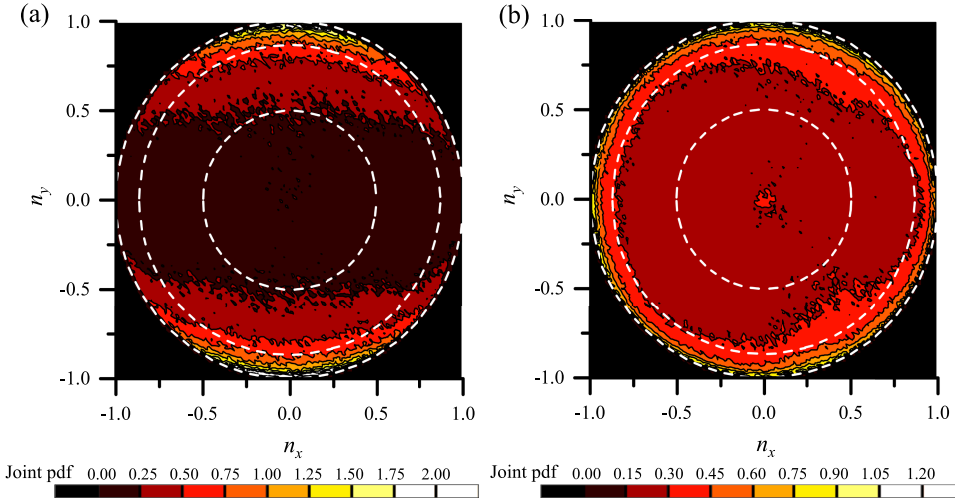


FIG. 5. Joint pdf of x and y direction components (n_x and n_y) of irrotational boundary unit normal vector $\mathbf{n} = (n_x, n_y, n_z)$ in (a) SFT and (b) PJET. The three white broken lines indicate $\cos \theta \equiv |n_z| = \sqrt{1 - n_x^2 - n_y^2}$ for $\theta = 30^\circ, 60^\circ$, and 90° (from the inner line toward the outer line), where θ is the angle between \mathbf{n} and the z direction.

enstrophy is concentrated in the core of these eddy structures. In contrast, concave regions are formed at the periphery of, or between, the vortices and are therefore expected to be associated with relatively smaller levels of enstrophy. As we will see below, the particular topology of the enstrophy near the TNTI also explains the enstrophy production in relation to the IB shape, which is the topic of Sec. III C.

C. The relation between the interface geometry and enstrophy and relative velocity

The relation between enstrophy production and the (i) shape, (ii) direction, and (iii) relative velocity near the IB is analyzed in detail. The reason to focus on the enstrophy production comes from the fact that this quantity dominates the flow in the TSL, and this layer probably displays different features in TSL from different flow types, since within this layer different eddy structures are observed depending on the flow type (e.g., wakes, jets, mixing layers, and boundary layers). Notice that unlike Wolf *et al.*,¹⁷ in which the dependence of the vorticity dynamics on the IB curvature was investigated right at the IB ($y_1 = 0$), we investigate the

enstrophy production in the nearby TSL ($y_1/\lambda = -0.25$) because the enstrophy production is negligibly small at the IB.

1. Interface geometry and enstrophy production

The relationship between the large-scale mean curvature and the enstrophy production in the nearby TSL (at $y_1/\lambda = -0.25$) can be appreciated in Fig. 7, showing the conditional joint pdf of $-H$ and P_ω at $y_1/\lambda = -0.25$ for SFT and PJET. The joint pdf is very similar for both flows and clearly shows that the enstrophy production term is larger for a convex ($-H < 0$) than for concave ($-H > 0$) shapes of the IB. Specifically, a maximum probability is observed in both flows for $-H\lambda \approx -1$.

The above result can be explained simply by the particular topology of the enstrophy magnitude in relation to the shape of the IB as discussed in Fig. 4. Indeed, enstrophy production is proportional to the enstrophy and we confirmed that the enstrophy production divided by enstrophy $P_\omega/(\omega^2/2)$ hardly depends on the large-scale mean curvature. Therefore, strong enstrophy production observed near convex IB regions is related to the large enstrophy content existing in this region,

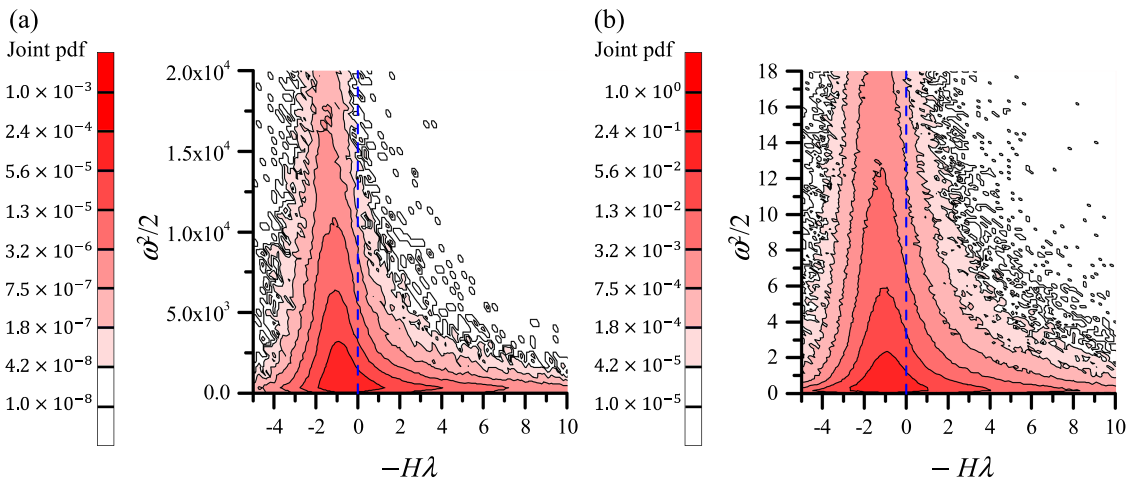


FIG. 6. Conditional joint pdf of large-scale mean curvature H and enstrophy $\omega^2/2$ at $y_1/\lambda = -0.25$ (turbulent sublayer) in (a) SFT and (b) PJET.

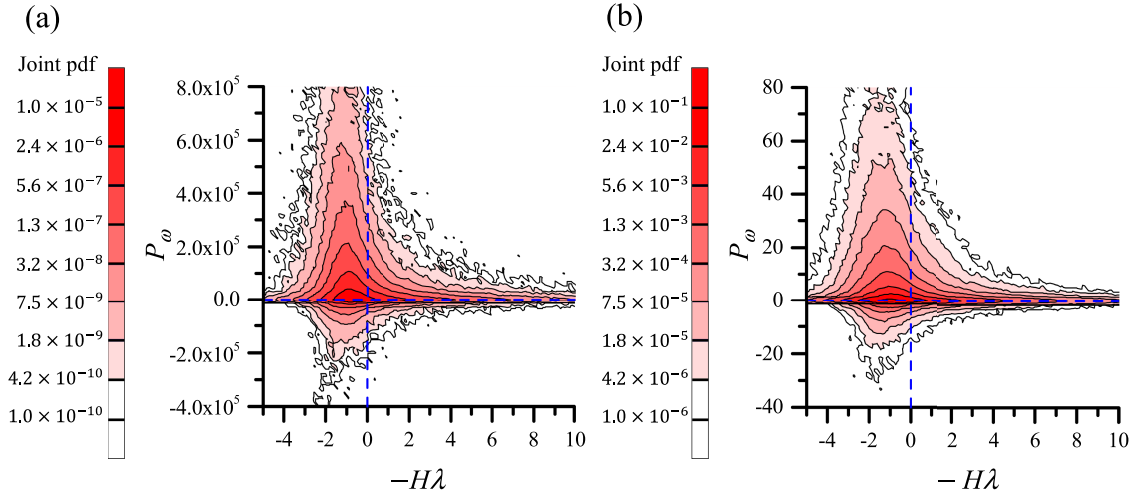


FIG. 7. Conditional joint pdf of large-scale mean curvature H and enstrophy production term P_ω at $y_1/\lambda = -0.25$ (turbulent sublayer) in (a) SFT and (b) PJET.

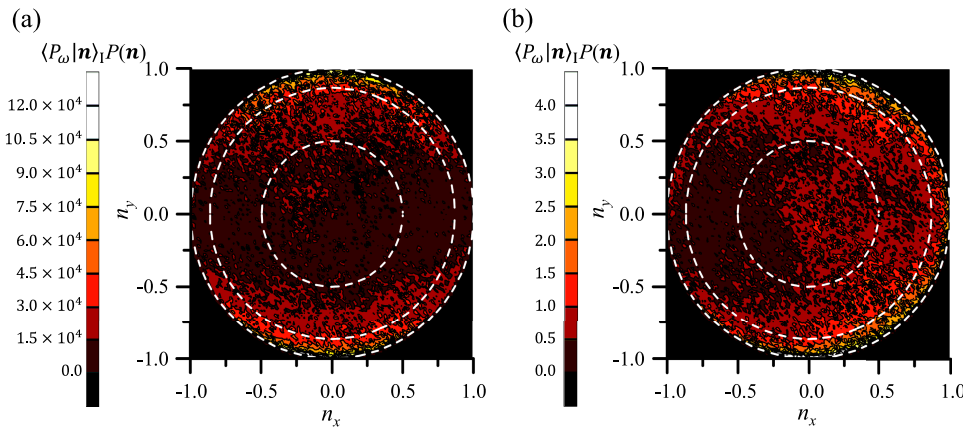


FIG. 8. Conditional average of enstrophy production term P_ω conditioned on the irrotational boundary unit normal vector $\mathbf{n} = (n_x, n_y, n_z)$ at $y_1/\lambda = -0.25$ (turbulent sublayer) in (a) SFT and (b) PJET. The conditional average $\langle P_\omega | \mathbf{n} \rangle_I$ is premultiplied by the pdf of \mathbf{n} , $P(\mathbf{n})$, so that the integration of the plot yields the average $\langle P_\omega \rangle_I$. The white broken lines are the same as in Fig. 5.

as also suggested by the strong similarity between Figs. 6 and 7.

The relation between the interface orientation and the enstrophy production within the nearby TSL is analyzed through Fig. 8 showing the average of P_ω conditioned on the irrotational boundary unit normal vector \mathbf{n} , $\langle P_\omega | \mathbf{n} \rangle_I$, at $y_1/\lambda = -0.25$. $\langle P_\omega | \mathbf{n} \rangle_I$ is premultiplied by the pdf of \mathbf{n} , $P(\mathbf{n})$, so that the integration of the plot yields $\langle P_\omega \rangle_I$. As in Fig. 5, $\langle P_\omega | \mathbf{n} \rangle_I P(\mathbf{n})$ is shown against n_x and n_y while n_z is related to n_x and n_y by $|\mathbf{n}| = 1$. In the PJET, the enstrophy production tends to be small for negative n_x , which agrees with previous DNS studies on spatially developing planar jets,^{15,34} since in these studies it has been shown that the enstrophy production is small near the interface when \mathbf{n} points in the upstream direction. For $\langle P_\omega | \mathbf{n} \rangle_I$ in SFT, we cannot see a clear dependence of the enstrophy production on the interface orientation, unlike in the PJET. Thus, again we observe that the interface orientation effects of P_ω depend on the flow configuration.

Consistently with Fig. 8, Fig. 9 shows the conditional pdf of P_ω conditioned on the sign of n_x at $y_1/\lambda = -0.25$ in PJET. The enstrophy positive production $P_\omega > 0$ and negative production $P_\omega < 0$ are, respectively, stronger and less intense when the IB faces the streamwise direction ($n_x > 0$), while the opposite trend can be observed for the IB regions facing the upstream region ($n_x < 0$).

2. Interface geometry and relative fluid velocity

As shown in Ref. 34, the turbulent fluid motion relative to the IB boundary movement affects the enstrophy production near the interface, via the alignment between the vorticity and strain-rate eigenvectors. The velocity of the IB movement, \mathbf{U}^I , is the sum of the velocity of the fluid $\mathbf{U}(\mathbf{x}_0^I)$ and the propagation velocity of the IB, \mathbf{V}^P , also known as the *local entrainment velocity*: $\mathbf{U}^I = \mathbf{U}(\mathbf{x}_0^I) + \mathbf{V}^P$, where $\mathbf{x} = \mathbf{x}_0^I$ represents the location of the IB. The propagation velocity of a given (constant) vorticity magnitude iso-surface is given

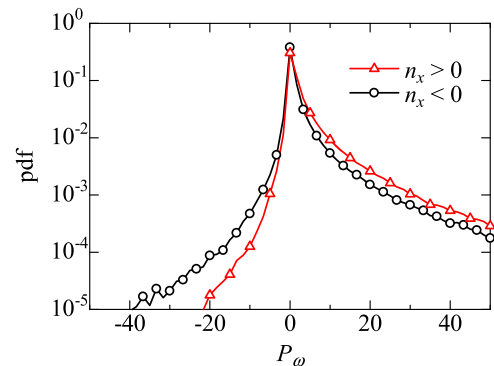


FIG. 9. Pdf of enstrophy production term P_ω conditioned on the sign of n_x at $y_1/\lambda = -0.25$ (turbulent sublayer) in the PJET.

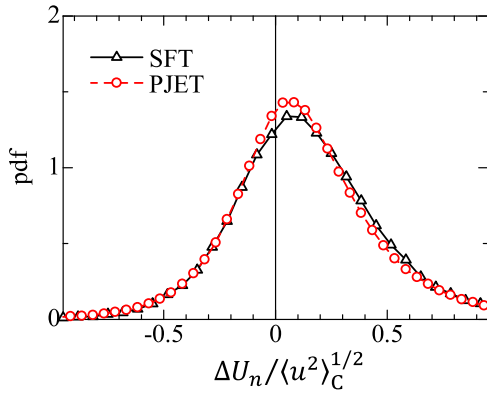


FIG. 10. Conditional pdf of relative velocity in the irrotational boundary normal direction, ΔU_n , at $y_1/\lambda = -0.5$ in SFT and PJET. The relative velocity is normalized by the root-mean-square of the streamwise velocity at the center of the turbulent core region ($y = 0$), $\langle u^2 \rangle_C^{1/2}$.

by²⁴

$$\mathbf{V}^P = \left(\frac{2\omega_i \mathcal{S}_{ij} \omega_j}{|\nabla \omega^2|} + \frac{2\nu \omega_i \nabla^2 \omega_i}{|\nabla \omega^2|} \right) \mathbf{n}. \quad (2)$$

Therefore, the fluid velocity at the location \mathbf{x} relative to the irrotational boundary movement is given by $\Delta \mathbf{U}^I = \mathbf{U}(\mathbf{x}) - \mathbf{U}^I = \mathbf{U}(\mathbf{x}) - \mathbf{U}(\mathbf{x}_0^I) - \mathbf{V}^P$. The relative velocity also plays an important role in the entrainment within the TNTI layer and is related to the entrainment velocity.³⁵ The relative velocity in the boundary normal direction is $\Delta U_n = \Delta \mathbf{U}^I \cdot \mathbf{n}$, where the relative velocity is calculated on the local coordinate y_1 using \mathbf{U}^I at $y_1 = 0$. Notice that for turbulent fluid approaching the IB, $\Delta U_n > 0$, whereas $\Delta U_n < 0$ represents turbulent fluid moving away from the IB.

Figure 10 shows the pdf of ΔU_n at $y_1/\lambda = -0.5$ in SFT and PJET, at which the conditional mean enstrophy reaches the turbulent core value (see Fig. 2). The pdf of normalized ΔU_n is similar in SFT and PJET, indicating that the relative velocity at this location scales with the root-mean-square (rms) velocity associated with large-scale motions, instead of the Kolmogorov velocity $u_\eta = (\epsilon\nu)^{1/4}$ associated with viscous effects. The propagation velocity is of the order of the Kolmogorov velocity,^{8,18,24} and thus, the fluid velocity difference

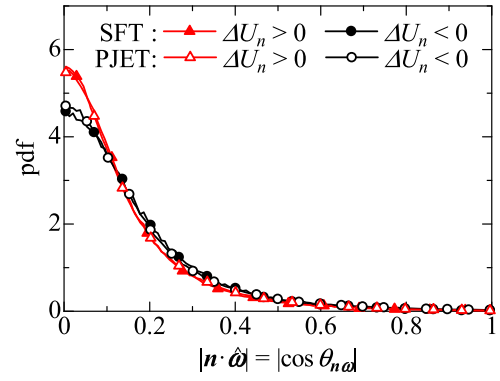


FIG. 11. Conditional pdf of cosine of angle between the irrotational boundary unit normal vector \mathbf{n} and the unit vorticity vector $\hat{\omega}$ ($\cos \theta_{n\omega}$) at $y_1/\lambda = -0.25$ (turbulent sublayer) in the SFT and PJET. The pdf is calculated conditioned on the sign of the relative velocity ΔU_n at $y_1/\lambda = -0.5$.

$\mathbf{U}(\mathbf{x}) - \mathbf{U}(\mathbf{x}_0^I)$ has a larger contribution to the relative velocity at $y_1/\lambda = -0.5$ than the propagation velocity \mathbf{V}^P . Moreover, although the pdf displays a maximum for $\Delta U_n > 0$ (fluid approaching the IB), many events of $\Delta U_n < 0$ (fluid moving away from the IB) are also observed.

Figure 11 shows the pdf of the cosine of the angle between the vorticity vector and irrotational boundary normal vector at $y_1/\lambda = -0.25$. As in previous studies on the TNTI,^{19,34} the vorticity is tangentially aligned with the irrotational boundary independently of the turbulent fluid motion; however, interestingly, this alignment is stronger near regions where the fluid motion is directed towards the IB $\Delta U_n > 0$ than moving away from the IB $\Delta U_n < 0$, again reflecting different interface geometries depending on the nearby velocity field.

The relation between the relative velocity and the interface geometry can be appreciated in Figs. 12 and 13 showing the joint pdf of (n_x, n_y) at the IB conditioned on the sign of ΔU_n at $y_1/\lambda = -0.5$ for SFT and PJET, respectively. For SFT, the pdfs for $\Delta U_n > 0$ and $\Delta U_n < 0$ are similar to the unconditional pdf shown in Fig. 5(a), and there is no particular relationship between the interface orientation and the relative velocity. In contrast, in PJET, the TNTI frequently faces the streamwise

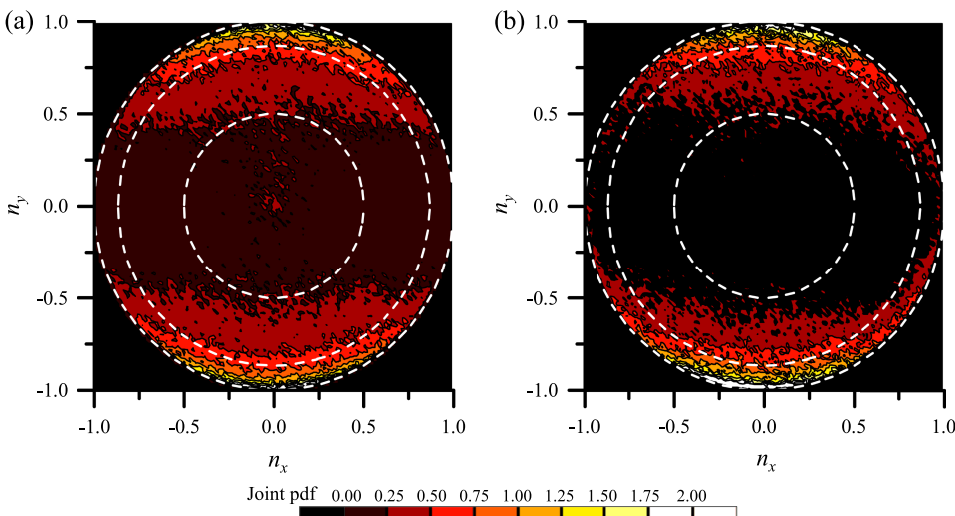


FIG. 12. Joint pdf of x and y direction components (n_x and n_y) of the irrotational boundary unit normal vector $\mathbf{n} = (n_x, n_y, n_z)$ in SFT calculated for (a) $\Delta U_n > 0$ and (b) $\Delta U_n < 0$. Three white broken lines are the same as in Fig. 5.

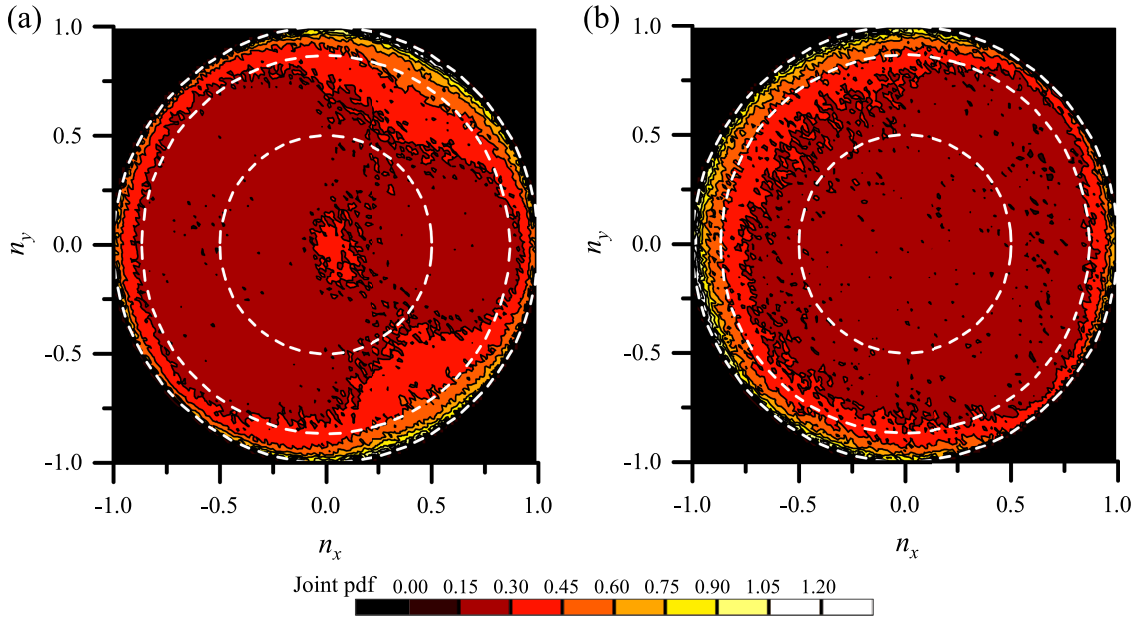


FIG. 13. Joint pdf of x and y direction components (n_x and n_y) of the irrotational boundary unit normal vector $\mathbf{n} = (n_x, n_y, n_z)$ in PJET calculated for (a) $\Delta U_n > 0$ and (b) $\Delta U_n < 0$. Three white broken lines are the same as in Fig. 5.

direction ($n_x > 0$) for $\Delta U_n > 0$, and the upstream region ($n_x < 0$) for $\Delta U_n < 0$, which shows that different flow configurations, and in particular, the existence of a mean shear influences the geometry of the TNTI in its relation to the entrainment velocity.

IV. THE INTENSE VORTICITY STRUCTURES NEAR THE TNTI

Since the TNTI is formed around the turbulent eddies from the turbulent core region, it is interesting to analyze the intense vorticity structures (IVSs) near the interface, particularly since the enstrophy production, which is crucial to the dynamics of the IVS, is related to the geometry of the TNTI. A detailed analysis of the IVS in planar jets was carried out in the work of da Silva *et al.*;²¹ however, in that work no comparison was made between the IVSs from different flow types nor was it studied in relation to the TNTI geometry.

The IVSs are detected and tracked using the same procedure described in the work of da Silva *et al.*²¹ Specifically, the IVS cores are extracted as regions with $|\omega| \geq \omega_I$, where ω_I is determined so that the core regions of the IVSs

occupy 1% of the turbulent volume. For each IVS, the core radius R , azimuthal velocity u_0 , and circulation Reynolds number $Re_\Gamma = \Gamma_0/\nu$ are calculated directly from the velocity and vorticity field,²¹ where the circulation is given by $\Gamma_0 = 2\pi R u_0$.

Figure 14 shows the conditional mean profiles of R , u_0 , and Re_Γ for SFT and PJET. Deep inside the turbulent region, the mean core radius in both SFT and PJET is about $4\eta \sim 5\eta$, which is similar to those observed in various flows.^{21,36–38} For PJET, R , u_0 , and Re_Γ increase towards the TNTI and drop sharply from $y_I/\eta \approx -10$, in agreement with previous works,²¹ whereas in SFT, a similar trend can be observed for R and Re_Γ , while u_0 is roughly constant for $y_I/\eta < -20$. We also expect that the radius of the IVS near the TNTI scales with the Kolmogorov length scale even at different Re just as deep inside the turbulent core region.^{36,37}

To examine the interface orientation dependence of the IVS characteristics, Fig. 15 shows the conditional average of R , u_0 , and Re_Γ calculated for $n_x > 0$ and $n_x < 0$ in PJET. The ratio between the core radius and the Burgers radius is also shown, as $\langle R_{BV} \rangle_I = \langle 2(\nu/\sigma)^{1/2} \rangle_I$, where $\sigma = \omega_i S_{ij} \omega_j / \omega_k \omega_k$ is the stretching rate of each IVS. Recall that the core radius of a

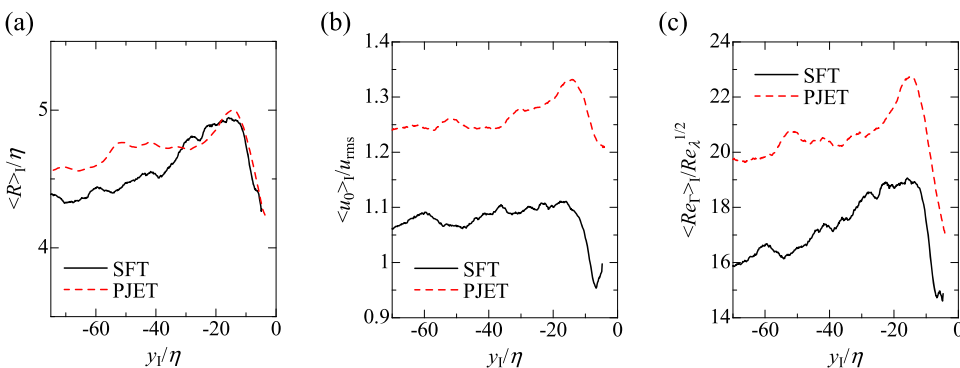


FIG. 14. Conditional profiles of IVS characteristics in SFT and PJET: (a) vortex core radius $\langle R \rangle_I / \eta$; (b) azimuthal velocity $\langle u_0 \rangle_I / u_{rms}$; (c) circulation Reynolds number $\langle Re_\Gamma \rangle_I / Re_\lambda^{1/2}$.

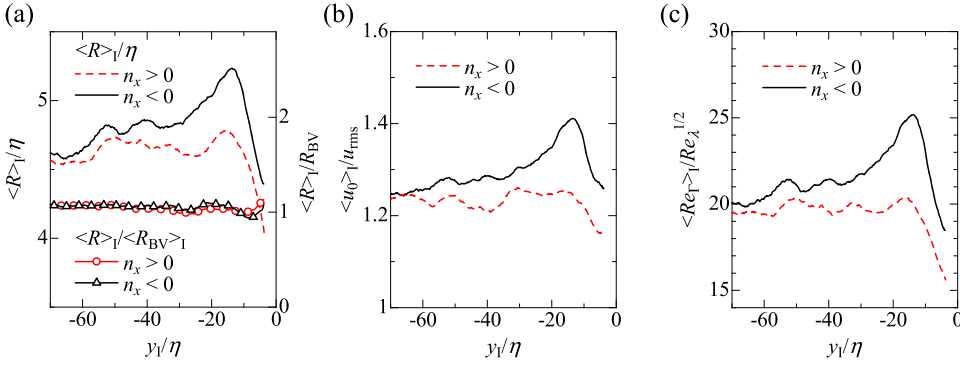


FIG. 15. Conditional profiles of IVS characteristics in PJET conditioned on the sign of n_x : (a) vortex core radius $\langle R \rangle_1$ normalized by η or the Burgers vortex radius estimated as $\langle R_{BV} \rangle_1 = \langle 2(\nu/\sigma)^{1/2} \rangle_1$, where σ is the axial stretching rate at the axis of the IVS; (b) azimuthal velocity $\langle u_0 \rangle_1 / u_{rms}$; (c) circulation Reynolds number $\langle Re_\Gamma \rangle_1 / Re_\lambda^{1/2}$.

Burgers vortex is kept constant by a balance between the vortex stretching, caused by the nearby large scale eddy motions, and enstrophy viscous diffusion. Interestingly, as in the work of da Silva *et al.*,²¹ we see that throughout all the flow, the IVSs are well described by the Burgers vortex model since $\langle R \rangle_1 \approx \langle R_{BV} \rangle_1$ for both $n_x > 0$ and $n_x < 0$ (Fig. 15). However, as the IVS approaches the IB, R , u_0 , and Re_Γ become quite different for $n_x > 0$ and $n_x < 0$. Specifically, higher values are obtained for $n_x < 0$ than for $n_x > 0$, which shows that the dynamics of the IVS is related to the orientation of the TNTI. Comparatively smaller R (as u_0 and Re_Γ) is observed for $n_x > 0$, precisely when positive enstrophy production (stretching) is larger and negative production (compression) is smaller (see Fig. 9). Conversely, the observed increase in R (as u_0 and Re_Γ) near the TNTI is consistent with smaller local values of enstrophy production (and a predominance of viscous diffusion), observed for $n_x < 0$ regions in Fig. 9. The present results clarify the observed variation of the IVS characteristics near the TNTI and show that the local TNTI

geometry also affects these intense vorticity structures such as IVSs.

V. DISCUSSIONS

In this section, we consider the difference in the enstrophy production within the TSL between SFT and PJET via the alignment characteristics of the vectors in this (sub)layer. The conditional statistics are calculated conditioned on the sign of ΔU_n at $y_1/\lambda = -0.5$ as in Sec. III C. At $y_1/\lambda = -0.25$, the pdfs of the cosine of the angles between \mathbf{n} and the strain-rate eigenvectors \mathbf{e}_i ($\cos \theta_{nei}$) and $\hat{\omega}$ and \mathbf{e}_i ($\cos \theta_{\omega ei}$) are calculated conditioned on the sign of ΔU_n (Figs. 16 and 17, respectively), where $\mathbf{e}_1 \geq \mathbf{e}_2 \geq \mathbf{e}_3$ and $\hat{\omega} = \boldsymbol{\omega}/|\boldsymbol{\omega}|$ is the unit vorticity vector. The angle between \mathbf{n} and \mathbf{e}_i significantly changes depending on ΔU_n : for the turbulent fluid approaching the irrotational boundary ($\Delta U_n > 0$), \mathbf{e}_1 shows a preference for the boundary tangential direction and \mathbf{e}_3 is parallel to the boundary normal direction while the opposite tendency is observed in

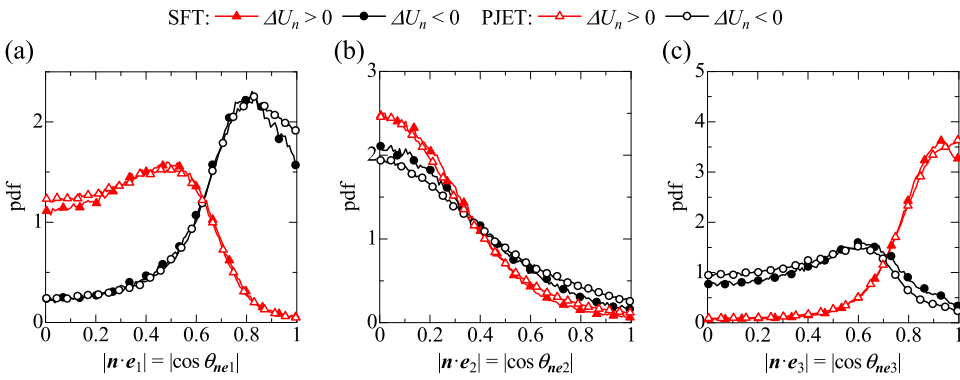


FIG. 16. Conditional pdf of cosine of angle between the irrotational boundary unit normal vector \mathbf{n} and the strain-rate eigenvector \mathbf{e}_i ($\cos \theta_{nei}$) at $y_1/\lambda = -0.25$ in the SFT and PJET: (a) extensive strain-rate eigenvector; (b) intermediate strain-rate eigenvector; (c) compressive strain-rate eigenvector. The pdf is calculated conditioned on the sign of the relative velocity ΔU_n at $y_1/\lambda = -0.5$.

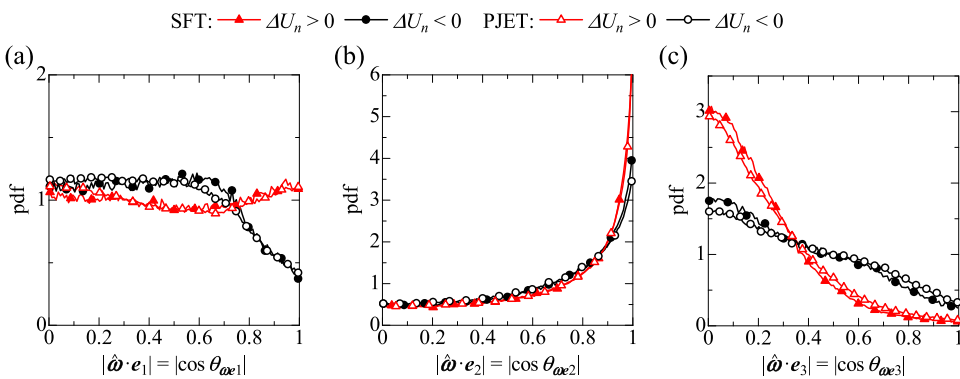


FIG. 17. Conditional pdf of cosine of angle between the unit vorticity vector $\hat{\omega}$ and the strain-rate eigenvector \mathbf{e}_i ($\cos \theta_{\omega ei}$) at $y_1/\lambda = -0.25$ in the SFT and PJET: (a) extensive strain-rate eigenvector; (b) intermediate strain-rate eigenvector; (c) compressive strain-rate eigenvector. The pdf is calculated conditioned on the sign of the relative velocity ΔU_n at $y_1/\lambda = -0.5$.

e_1 and e_3 for the turbulent fluid moving away from the irrotational boundary ($\Delta U_n < 0$). However, e_2 is frequently aligned with the tangential direction of the irrotational boundary independently of ΔU_n . Because the vorticity is tangentially aligned with the TNTI, the dependence of the eigenvectors on ΔU_n causes the difference in $\cos\theta_{\omega e_i}$ between the positive and the negative ΔU_n as shown in Fig. 17. Comparing these statistics on the alignments conditioned on the sign of ΔU_n , one can see that the vorticity hardly aligns with the eigenvector, which is orientated in the boundary normal direction (e_3 for $\Delta U_n > 0$ and e_1 for $\Delta U_n < 0$). The dependence of these alignments on the relative velocity can be seen both in the SFT and PJET. Thus, the observed difference in Fig. 8 can be attributed to the dependence of the alignments discussed above and to the relation between the interface orientation and the turbulent fluid motions, which strongly depend on the difference in the mean flow between the turbulent and non-turbulent regions, i.e., the existence of mean shear (Figs. 12 and 13). The present results show that the TNTI affects the behavior of nearby turbulence, where the alignments related to the dynamics and structure of turbulence³⁹ are different from the turbulent core region.

VI. CONCLUSION

The geometry of the turbulent/non-turbulent interface (TNTI) from planar jet (PJET) and shear free turbulence (SFT) was analyzed in relation to the enstrophy and relative velocity nearby, by using direct numerical simulations.

In both SFT and PJET, the TNTI is dominated by a convex shaped geometry, where the enstrophy nearby tends to be strong. However, whereas the TNTI in SFT faces preferentially the y direction, in PJET it tends to equally face the x and y directions.

In contrast to the SFT, where the velocity in relation to the irrotational boundary motion has no particular relation to the TNTI orientation, the TNTI in the PJET preferentially faces $n_x > 0$ when the turbulent fluid approaches the TNTI and $n_x < 0$ when the turbulent fluid moves away from the TNTI. Therefore, unlike in the SFT, the enstrophy dynamics in the turbulent sublayer in the PJET is strongly related to the interface orientation. Finally, the geometry of the TNTI in the PJET is also related to the intense vorticity structures since a decrease/increase in enstrophy production in TNTI regions facing $n_x < 0/n_x > 0$ leads to an increase/decrease in (among other characteristics) local radius of these structures. Thus, the geometrical influences on the TNTI are flow dependent and very different between the flows with and without mean shear.

ACKNOWLEDGMENTS

This work was partially supported by the Collaborative Research Project on Computer Science with High-Performance Computing in Nagoya University and by JSPS KAKENHI, Grant Nos. 16K18013 and 25289030. C. B. da Silva acknowledges Fundação para a ciência e a Tecnologia (FCT) under Grant No. PTDC/EMS-ENE/6129/2014.

- ¹S. A. Thorpe, "The near-surface ocean mixing layer in stable heating conditions," *J. Geophys. Res.* **83**, 2875, doi:10.1029/jc083ic06p02875 (1978).
- ²S. A. Thorpe, "Recent developments in the study of ocean turbulence," *Annu. Rev. Earth Planet. Sci.* **32**, 91 (2004).
- ³L. Mahrt, "Stratified atmospheric boundary layers," *Boundary-Layer Meteorol.* **90**, 375 (1999).
- ⁴A. W. Woods, "Turbulent plumes in nature," *Annu. Rev. Fluid Mech.* **42**, 391 (2010).
- ⁵T. H. Ellison and J. S. Turner, "Turbulent entrainment in stratified flows," *J. Fluid Mech.* **6**, 423 (1959).
- ⁶C. B. da Silva, J. C. R. Hunt, I. Eames, and J. Westerweel, "Interfacial layers between regions of different turbulence intensity," *Annu. Rev. Fluid Mech.* **46**, 567 (2014).
- ⁷A. Attili, J. C. Cristancho, and F. Bisetti, "Statistics of the turbulent/non-turbulent interface in a spatially developing mixing layer," *J. Turbul.* **15**, 555 (2014).
- ⁸M. Wolf, M. Holzner, B. Lüthi, D. Krug, W. Kinzelbach, and A. Tsinober, "Effects of mean shear on the local turbulent entrainment process," *J. Fluid Mech.* **731**, 95 (2013).
- ⁹D. Mistry, J. Philip, J. R. Dawson, and I. Marusic, "Entrainment at multi-scales across the turbulent/non-turbulent interface in an axisymmetric jet," *J. Fluid Mech.* **802**, 690 (2016).
- ¹⁰G. Borrell and J. Jiménez, "Properties of the turbulent/non-turbulent interface in boundary layers," *J. Fluid Mech.* **801**, 554 (2016).
- ¹¹S. Corrsin and A. L. Kistler, "Free-stream boundaries of turbulent flows," NACA Tech. Rep. **1244**, 1033 (1955).
- ¹²A. A. Townsend, *The Structure of Turbulent Shear Flow* (Cambridge University Press, 1976).
- ¹³M. Gampert, V. Narayanaswamy, P. Schaefer, and N. Peters, "Conditional statistics of the turbulent/non-turbulent interface in a jet flow," *J. Fluid Mech.* **731**, 615 (2013).
- ¹⁴C. B. da Silva, R. R. Taveira, and G. Borrell, "Characteristics of the turbulent/nonturbulent interface in boundary layers, jets and shear-free turbulence," *J. Phys.: Conf. Ser.* **506**, 012015 (2014).
- ¹⁵T. Watanabe, Y. Sakai, K. Nagata, Y. Ito, and T. Hayase, "Enstrophy and passive scalar transport near the turbulent/non-turbulent interface in a turbulent planar jet flow," *Phys. Fluids* **26**, 105103 (2014).
- ¹⁶J. C. LaRue and P. A. Libby, "Statistical properties of the interface in the turbulent wake of a heated cylinder," *Phys. Fluids* **19**, 1864 (1976).
- ¹⁷M. Wolf, B. Lüthi, M. Holzner, D. Krug, W. Kinzelbach, and A. Tsinober, "Investigations on the local entrainment velocity in a turbulent jet," *Phys. Fluids* **24**, 105110 (2012).
- ¹⁸R. Jahanbakhshi and C. K. Madnia, "Entrainment in a compressible turbulent shear layer," *J. Fluid Mech.* **797**, 564 (2016).
- ¹⁹C. B. da Silva and R. J. N. dos Reis, "The role of coherent vortices near the turbulent/non-turbulent interface in a planar jet," *Philos. Trans. R. Soc., A* **369**, 738 (2011).
- ²⁰C. B. da Silva and R. R. Taveira, "The thickness of the turbulent/nonturbulent interface is equal to the radius of the large vorticity structures near the edge of the shear layer," *Phys. Fluids* **22**, 121702 (2010).
- ²¹C. B. da Silva, R. J. N. Dos Reis, and J. C. F. Pereira, "The intense vorticity structures near the turbulent/non-turbulent interface in a jet," *J. Fluid Mech.* **685**, 165 (2011).
- ²²C. M. de Silva, J. Philip, K. Chauhan, C. Meneveau, and I. Marusic, "Multiscale geometry and scaling of the turbulent-nonturbulent interface in high Reynolds number boundary layers," *Phys. Rev. Lett.* **111**, 044501 (2013).
- ²³K. Chauhan, J. Philip, C. M. de Silva, N. Hutchins, and I. Marusic, "The turbulent/non-turbulent interface and entrainment in a boundary layer," *J. Fluid Mech.* **742**, 119 (2014).
- ²⁴M. Holzner and B. Lüthi, "Laminar superlayer at the turbulence boundary," *Phys. Rev. Lett.* **106**, 134503 (2011).
- ²⁵M. A. C. Teixeira and C. B. da Silva, "Turbulence dynamics near a turbulent/non-turbulent interface," *J. Fluid Mech.* **695**, 257 (2012).
- ²⁶C. B. da Silva and J. C. F. Pereira, "Invariants of the velocity-gradient, rate-of-strain, and rate-of-rotation tensors across the turbulent/nonturbulent interface in jets," *Phys. Fluids* **20**, 055101 (2008).
- ²⁷R. R. Taveira and C. B. da Silva, "Kinetic energy budgets near the turbulent/nonturbulent interface in jets," *Phys. Fluids* **25**, 015114 (2013).
- ²⁸C. B. da Silva and O. Métais, "On the influence of coherent structures upon interscale interactions in turbulent plane jets," *J. Fluid Mech.* **473**, 103 (2002).
- ²⁹T. Watanabe and K. Nagata, "Mixing model with multi-particle interactions for Lagrangian simulations of turbulent mixing," *Phys. Fluids* **28**, 085103 (2016).

- ³⁰R. R. Taveira and C. B. da Silva, "Characteristics of the viscous superlayer in shear free turbulence and in planar turbulent jets," *Phys. Fluids* **26**, 021702 (2014).
- ³¹D. K. Bisset, J. C. R. Hunt, and M. M. Rogers, "The turbulent/non-turbulent interface bounding a far wake," *J. Fluid Mech.* **451**, 383 (2002).
- ³²T. Watanabe, Y. Sakai, K. Nagata, Y. Ito, and T. Hayase, "Turbulent mixing of passive scalar near turbulent and non-turbulent interface in mixing layers," *Phys. Fluids* **27**, 085109 (2015).
- ³³R. R. Taveira, J. S. Diogo, D. C. Lopes, and C. B. da Silva, "Lagrangian statistics across the turbulent-nonturbulent interface in a turbulent plane jet," *Phys. Rev. E* **88**, 043001 (2013).
- ³⁴T. Watanabe, Y. Sakai, K. Nagata, Y. Ito, and T. Hayase, "Vortex stretching and compression near the turbulent/nonturbulent interface in a planar jet," *J. Fluid Mech.* **758**, 754 (2014).
- ³⁵T. Watanabe, C. B. da Silva, Y. Sakai, K. Nagata, and T. Hayase, "Lagrangian properties of the entrainment across turbulent/non-turbulent interface layers," *Phys. Fluids* **28**, 031701 (2016).
- ³⁶J. Jiménez and A. A. Wray, "On the characteristics of vortex filaments in isotropic turbulence," *J. Fluid Mech.* **373**, 255 (1998).
- ³⁷M. Tanahashi, S. Iwase, and T. Miyauchi, "Appearance and alignment with strain rate of coherent fine scale eddies in turbulent mixing layer," *J. Turbul.* **2**, N6 (2001).
- ³⁸R. Jahanbakhshi, N. S. Vaghefi, and C. K. Madnia, "Baroclinic vorticity generation near the turbulent/non-turbulent interface in a compressible shear layer," *Phys. Fluids* **27**, 105105 (2015).
- ³⁹A. Tsinober, *An Informal Conceptual Introduction to Turbulence* (Springer, 2009).